Received: 6 December 2023 | Revised: 16 April 2024 | Accepted: 24 April 2024

CAAI Transactions on Intelligence Technology

DOI: 10.1049/cit2.12351

ORIGINAL RESEARCH

WaveSeg-UNet model for overlapped nuclei segmentation from multi-organ histopathology images

Hameed Ullah Khan | **Basit Raza** | **Muhammad Asad Iqbal Khan** | **Muhammad Faheem**

Computer Science Department, Comsats University Islamabad, Islamabad, Pakistan

Correspondence
Muhammad Faheem, Department of Computing Science, School of Technology and Innovations, University of Vaasa, Vaasa 65200, Finland.
Email: muhammad.faheem@uwasa.fi

Abstract

Nuclei segmentation is a challenging task in histopathology images. It is challenging due to the small size of objects, low contrast, touching boundaries, and complex structure of nuclei. Their segmentation and counting play an important role in cancer identification and its grading. In this study, WaveSeg-UNet, a lightweight model, is introduced to segment cancerous nuclei having touching boundaries. Residual blocks are used for feature extraction. Only one feature extractor block is used in each level of the encoder and decoder. Normally, images degrade quality and lose important information during down-sampling. To overcome this loss, discrete wavelet transform (DWT) alongside max-pooling is used in the down-sampling process. Inverse DWT is used to regenerate original images during up-sampling. In the bottleneck of the proposed model, atrous spatial channel pyramid pooling (ASCPP) is used to extract effective high-level features. The ASCPP is the modified pyramid pooling having atrous layers to increase the area of the receptive field. Spatial and channel-based attention are used to focus on the location and class of the identified objects. Finally, watershed transform is used as a post processing technique to identify and refine touching boundaries of nuclei. Nuclei are identified and counted to facilitate pathologists. The same domain of transfer learning is used to retrain the model for domain adaptability. Results of the proposed model are compared with state-of-the-art models, and it outperformed the existing studies.

KEYWORDS

artificial intelligence, deep learning, machine learning, medical image processing

1 | INTRODUCTION

Histopathology has evolved as one of the important fields in the diagnosis of almost all kinds of diseases. Every year, millions of histopathology images are taken for treatment and these images provide vital information to histopathologists. Microscopic images are often stained with haematoxylin and eosin (H&E) [1]. Traditionally, pathologists manually segment nuclei of histopathology images. Manually counting of nuclei is tedious and a time-consuming task. Automated nuclei segmentation in histopathology images is an important element of computer-aided design systems (CADs). Optimised nuclei segmentation helps in accurate nuclei counting, which increases the performance of models [2].

Nuclei segmentation is a challenging task due to interclass homogeneity and intraclass heterogeneity [3]. One nucleus divides itself into two nuclei during the mitosis process. During this division, it changes its shape which increases their misclassification rate. Additionally, the segmentation of touching/overlapping nuclei is also a challenging task. Low-intensity differences between the foreground and background and vanishing boundaries are the misleading factors. CADs [4,

Hameed Ullah Khan, Basit Raza, Muhammad Asad Iqbal Khan, and Muhammad Faheem contributed equally to accomplish this research work.

5] are thought to be a more effective solution to handle these challenges.

Accurate nuclei segmentation is an important and challenging task for CADs in histopathology images [6]. The unavailability of large datasets makes it further challenging. Deep learning techniques [7, 8] are considered comparatively better approaches than conventional machine learning models [9–13]. These techniques have focused on deep features extraction to get accurate segmented nuclei. Various computer-aided techniques are used for segmentation and nuclei counting of microscopic images, and novel approaches are still being examined. Several techniques are used to segment overlapped [14, 15] and clustered nuclei [4, 16]. Some recent techniques [17–19] have provided a framework for microscopic object segmentation. However, small, cluster-based complex heterogeneous nuclei segmentation remained an issue for various techniques.

In the proposed model, we are addressing the challenges associated with nuclei segmentation in histopathology images. Accurate identification and counting of nuclei are the fundamental requirements for cancer grading. Existing studies face difficulties identifying nuclei due to the small size of nuclei, low foreground and background contrast, and touching boundaries of nuclei. To overcome these challenges, the WaveSeg-UNet, a lightweight model, is introduced specifically to segment nuclei with touching boundaries. In the proposed model, residual blocks are used for feature extraction and discrete wavelet transform (DWT) is utilised to mitigate information loss during down-sampling. The atrous spatial channel pyramid pooling (ASCPP) having spatial and channel-based attention mechanisms is employed for high-level feature extraction. Additionally, the same domain of transfer learning is utilised to enhance model adaptability. By improving segmentation accuracy and efficiency, the proposed model aims to facilitate pathologists in cancer segmentation and grading. The ultimate contribution of more accurate segmentation is to increase the survival chances of cancer-affected individuals. This study has the following contributions.

- WaveSeg-UNet, a lightweight model, is proposed to identify and refine touching boundaries of small nuclei and segment them for accurate counting of nuclei in histopathology images. The same domain of transfer learning is used to evaluate the proposed model.
- DWT and inverse discrete wavelet transform (IDWT) are used in hybrid down-sampling and hybrid up-sampling, respectively, to preserve the spatial localisation of features in an image.
- The proposed WaveSeg-UNet model employs a combination of atrous spatial and channel attention-based pyramid pooling (ASCPP) to detect small objects. The atrous layers enlarge small objects, while spatial attention helps to locate the object and channel attention helps to identify the object class.
- To accurately count the segmented nuclei, watershed transformation is applied as a post-processing technique to identify and refine the boundaries of touching/overlapped nuclei.

In the rest of the paper, related work is discussed in Section 2. In this section, we provided a detailed review of the existing literature and highlighted the gaps that our study aims to fill. Section 3 describes the method used in our research, including datasets and the proposed model. We presented our results and discussions in Section 4. Finally, in Section 5, we provided the conclusion of our study, as well as recommendations for the future research work.

2 | RELATED WORK

Conventional segmentation models primarily depend on traditional methods, such as active contour variants, morphological operations, and colour-based thresholding [20, 21]. These techniques, however, cannot generalise nuclei morphology [4]. Furthermore, the segmentation of touching and overlapped nuclei remained an issue for these techniques [7, 22]. Conventional machine learning techniques such as SVM and random forest use hand-crafted features for nuclei segmentation [23–27]. The performance of the traditional machine learning techniques suffers due to low domain knowledge during feature extraction [28–31].

The study [32] treated nuclei identification as a segmentation task, while another study [33] treated it as a regression task by applying a nuclei distance map. Another study [34] found that nuclei segmentation through multi-model fusion is better than multi-task learning and stand-alone models. Several strategies [28] and [35] used CNN-based models to predict objects and their contours, while another study [36] introduced U-Net++ as a multiple U-Net-based model with redefined skip connections. These models are not capable enough to handle small nuclei, touching boundaries, inter-class homogeneity, and intra-class heterogeneity.

A two-step nuclei segmentation method is introduced by Yi et al. [37] where the SSD model is utilised to obtain and crop the bounding box patches, and in the second step, instance segmentation is performed. The region-based convolutional network [38] is introduced to detect and segment nuclei. An encoder–decoder network [39] with the integration of residual block, attention block, and bottleneck layer is introduced to minimise the information loss during the pooling layer. The encoder–decoder approach [40] with atrous spatial pyramid pooling model, dilated residual network [41], and small mitotic detector [42] is proposed to increase the results of nuclei identification. The multi-scale fully convolutional residual network with dilated layers [43] is introduced for the segmentation of histological images. These techniques are helpful in overcoming challenges such as the disappearance of small objects, the correct localisation of small objects, and segmentation of complex nuclei.

Several deep learning approaches [15, 40, 44] are used to specifically segment out overlapped/touching nuclei. In research [15], DenseRes-Unet is proposed where dense blocks are integrated in the final layer of the encoder for diverse information. Semantic gap is one of the major issues between the encoder and decoder path, so atrous blocks in skip connections are used to reduce this gap. Distance map is applied for centre point detection to identify overlapped nuclei accurately. On the other hand, modified atrous spatial pyramid pooling in U-Net (ASPPU-Net) [40] is used to handle the heterogeneity of nuclei for better feature extraction without affecting spatial resolution in histopathology images. This model utilised a concave point detection technique after atrous convolution bottleneck to refine and split touching boundaries of nuclei. The synchronous segmentation method [45] is introduced to identify the overlapped nuclei, where identified nuclei are refined using vertical and horizontal centre-point separation methods. Finally, contour-seed learning [14] is utilised for the segmentation of refined touching nuclei.

A model is introduced in the study [46] which can segment, detect, and classify the objects at the same time. The detection and classification of models are performed based on centre key-points of objects. The joint pyramid fusion module is also introduced to enhance local features to help classification and detection. Model is evaluated on four datasets including the PanNuke, MonuSeg, TNBS, and BBBC039V1 dataset. It is a diverse model which outperformed the existing studies. Another study [47] is also evaluated on the same dataset. It is a multi-stage model which introduces instance nuclei segmentation and classification, simultaneously. It is the less complex model as compared to the previous study. These models can face generalisation problems as these are trained on a single dataset. To overcome these issues, the authors in Ref. [48] introduced the multi-task learning model. The generalisation of the model is ensured by evaluating over 600 thousand segmentation and 440 thousand classification samples. It is evaluated on various organs having millions of nuclei. Triple U-net [49] is a model which has three branches. The RGB branch, segmentation branch, and haematoxylin branch are used to extract rich features. To generalise the model, it is validated on three datasets. Due to three feature extraction branches, it is a complex model.

3 | METHODOLOGY

Cancer identification through histopathology images is a gold standard. However, it has some challenges due to the complexity of histopathology images. Histopathology images have the challenges of low contrast, inter-class homogeneity, intra-class heterogeneity, unavailability of large datasets, disappearance of small nuclei, and identification of touching boundaries in clustered nuclei. State-of-the-art CADs with some limitations are used for early and accurate cancer identification. In this study, we introduced the WaveSeg-UNet model for the accurate segmentation of clustered nuclei having overlapped/touching boundaries.

3.1 | Datasets

We evaluated the proposed model on three publicly available datasets. These datasets are Triple negative breast cancer (TNBC), BBBC039V1, and PanNuke.

3.1.1 | Triple negative breast cancer

It is a breast cancer dataset which is collected from seven patients. It has 50 images of size 512 × 512 pixels. These images are taken at a 40× magnification level. It has 4022 annotated nuclei. On average, each image has 80 nuclei, and the minimum number of nuclei in an image is 5.

3.1.2 | BBBC039V1

BBBC039 (Broad Bioimage Benchmark Collection 039) is a publicly available microscopic dataset of breast cancer. It is a segmentation and classification dataset. This dataset has 200 TIFF files of size 520 × 696 each. This dataset has a total of 23,000 nuclei.

3.1.3 | MoNuSeg

MoNuSeg is the multi organ histopathology dataset for image segmentation. These images are taken under a 40× magnification level. Images of this dataset have size of 1000 × 1000. It is a diverse dataset of seven organs including Bladder, Breast, Colon, Kidney, Liver, Prostate, and Stomach. Images of this dataset are collected from 30 patients.

3.1.4 | PanNuke

PanNuke is a pan-cancer segmentation dataset of 19 organs [50, 51]. Whole-slide images of this dataset are divided into 256 × 256 × 3 sized patches. This dataset has around 200 k nuclei having five categories, excluding the background. This dataset is the advancement of the MoNuSeg [22] dataset. In the PanNuke dataset, samples are labelled for both semantic and instance segmentation. Five categories of the dataset with their number of nuclei are Inflammatory (32,276), Connective (50,585), Neoplastic (77,403), Non-neoplastic Epithelial (26,572), and Dead (2908). Nineteen organs with the number of nuclei are Breast (51,077), Colon (35,711), Bile-duct (9048), Oesophagus (9292), Uterus (8791), Lung (7071), Cervix (7288), Head-Neck (7789), Skin (7081), Adrenal gland (6948), Kidney (4426), Stomach (5408), Prostate (4175), Testis (4723), Liver (4890), Thyroid (4896), Pancreatic (4434), Ovarian (3857), and Bladder (2839).

3.2 | Proposed model

One of the major causes of misclassification and miscounting of objects in histopathology is overlapping/touching boundaries of nuclei. To address this problem, the WaveSeg-UNet, a segmentation model, is introduced. Accurate boundaries identification and refinement lead to better performance of models. The 256 × 256 sized images are used as input of the proposed domain adaptive WaveSeg-UNet model. The

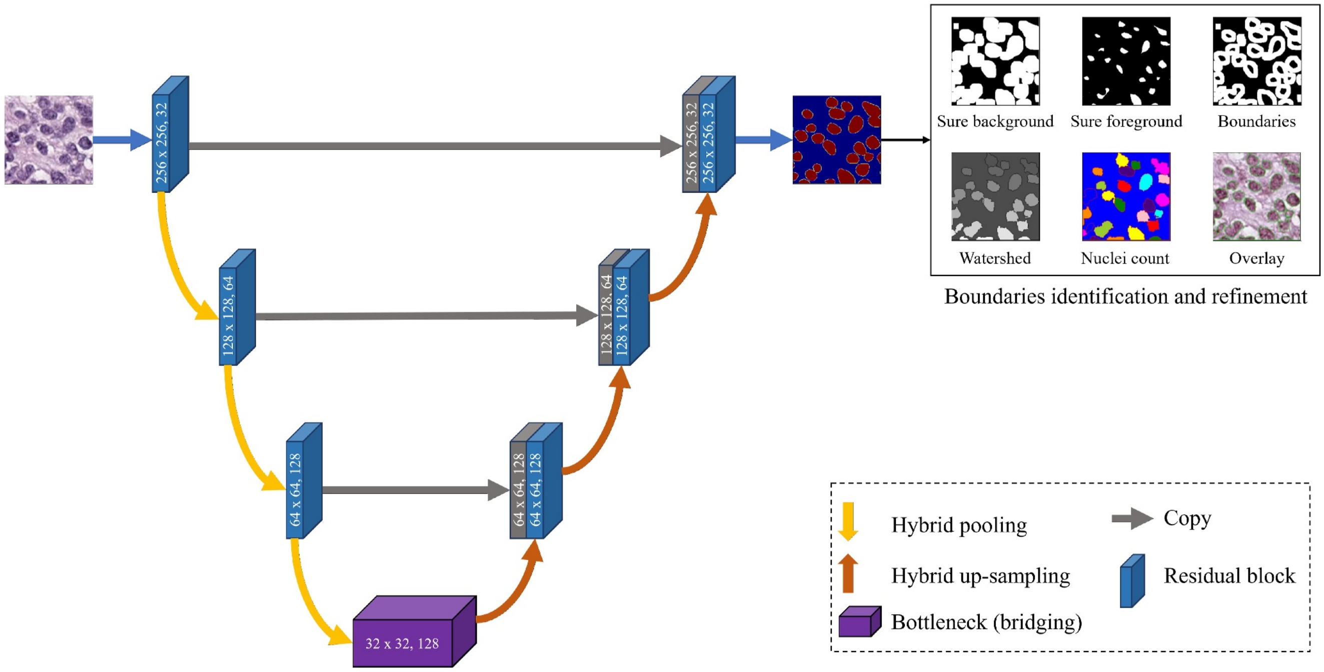

FIGURE 1 The proposed WaveSeg-UNet model.

proposed model employs residual blocks as a feature extractor, as demonstrated in Figure 1. The hybrid pooling layer is used during the down-sampling process of the model. The ASCPP bottleneck block is used as a bridging block between the down-sampling and the up-sampling of the model. A hybrid up-sampling technique is integrated into the model to achieve a better segmentation of small objects. In the proposed model, the watershed technique is applied as a post processing technique where the distance map is applied. It assists the proposed segmentation model to identify touching boundaries of nuclei in histopathology images.

3.2.1 | Pre-processing

In histopathology images, complexity, variation in the staining process, and noise are the reasons for the low performance of models. Contrast limited adaptive histogram equalisation is used as a pre-processing technique to enhance the contrast of the foreground and background. It is a small window-based contrast enhancement technique, whereas others are image-based enhancement techniques. This window-based technique is useful for blurry and occluded small objects. A window of size (8, 8) is applied on the images of small nuclei.

Histopathology images from the PanNuke dataset have a size of 256 × 256 × 3 pixels. Other datasets have large scale images. The proposed model accepts images of 256 × 256 × 3 as input. Since both the PanNuke samples and the model input are of the same size, cropping or resizing has not been performed for it. We cropped the images of other datasets accordingly. For model evaluation, the datasets are divided into train, validation, and test sets, comprising 70%, 20%, and 10% of the data samples, respectively.

3.2.2 | Domain adaptation

Deep learning models require large datasets for their evaluation. Lack of large datasets is one of the main issues of medical imaging, particularly in histopathology. Transfer learning is one of the techniques used to overcome this issue. However, microscopic images have different structures and shape of objects as compared to natural images, so transferring of weights from natural to microscopic images leads towards domain adaptation issues. This transferring technique does not provide the required impact on the performance of the model. To gain the better impact of transfer learning, the same domain of transfer learning is adapted in the proposed model. Initially, the model is trained on a microscopic dataset BBBC039V1 to obtain pre-trained weights of the same domain. Subsequently, the weights of the same domain are transferred for retraining the model. Comparatively, the same domain of transfer learning provided better results than different domains of transfer learning with a smaller number of epochs.

3.2.3 | Feature extraction

Deep neural networks are useful models to extract local as well as global features. In this study, residual blocks are used to extract features as shown in Figure 2. Identity connections of residual networks make them superior over other feature extractors to overcome the vanishing gradient issue. Various

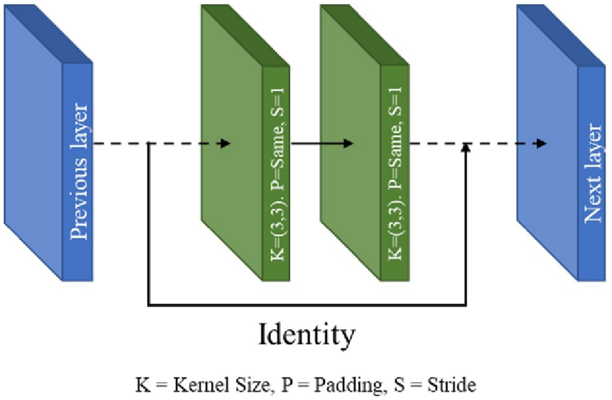

FIGURE 2 Residual block: The feature extraction block based on two layers with identity connection.

convolutional layers in a residual block are used in different studies; however, in the proposed model, residual blocks having two convolutional layers are used for feature extraction. In both the encoder and decoder of U-net, one residual block is used on each level of the proposed model. Relu activation function, same padding, filter size of 3 × 3, stride of 1 and HE normal are used in the proposed feature extractor. Equation (1) shows the additive method (+) of skip connection and convolutional layers of a residual block.

$$\mathrm{H(x) = f(wx + b) + x} \tag{1}$$

'w' represents the weight vector, 'x' is used for the number of inputs, and 'b' represents bias which is a small value associated with every input. In Equation (1), additional 'x' shows the additive property of skip connection. This property makes the model capable of extracting rich features by adding feature maps of previous layers.

3.2.4 | Hybrid pooling

Pooling layers help to reduce dimensions of the image to extract global features of succeeding convolutional layers. In the proposed model, a hybrid of max-pooling and DWT is introduced. Hybrid pooling is useful for the succeeding layers to extract diverse features that leads towards better performance of the model. The max-pooling layer generates information based on neighbourhood as shown in Equation (2). In max-pooling, the maximum value is taken from the specific region.

$$\mathrm{z_{kpq}} = \max_{(i,j)\in R_{pq}} \left(z_{kij}\right) \tag{2}$$

R_{pq} is the region, whereas z_{kij} is the input at (i, j). z_{kpq} is the output of z_{kij} activation at the 'k' feature map.

Discrete wavelet transform is used to minimise the impact of neighbourhood reduction [52]. It is a data compression-based image reduction technique. Images compressed/reduced through this technique can be reconstructed using IDWT without losing information. This technique also lowers the chance of rough edge detection which leads towards a high accuracy of small object segmentation. The last channel of the second level DWT is used in the proposed model. Invertible matrices f_{LL}, f_{LH}, f_{HL}, and f_{HH} of dimensions 4 × 4 are used as shown in Equation (3). The DWT has four operations over these invertible matrices. Those operations are z_{LL}, z_{LH}, z_{HL}, and z_{HH}.

$$f_{LL} = \begin{bmatrix} 1 & 1 \\ 1 & 1 \end{bmatrix}, f_{LH} = \begin{bmatrix} -1 & -1 \\ 1 & 1 \end{bmatrix}, \\ f_{HL} = \begin{bmatrix} -1 & 1 \\ -1 & 1 \end{bmatrix}, f_{HH} = \begin{bmatrix} 1 & -1 \\ -1 & 1 \end{bmatrix} \tag{3}$$

The down-sampling and output of DWT are calculated by the convolution operation of invertible matrices. In this study, the down-sampling factor $' \downarrow '$ of 2 is used. DWT matrices $z_{LL} = (f_{LL} \otimes z) \downarrow 2$, $z_{LH} = (f_{LH} \otimes z) \downarrow 2$, $z_{HL} = (f_{HL} \otimes z) \downarrow 2$, and $z_{HH} = (f_{HH} \otimes z) \downarrow 2$ are further explained in Equations (4–7). $\otimes$ is the convolution operator.

$$z_{LL}(p,q) = z(2p-1, 2q-1) + z(2p-1, 2q) \\ + z(2p, 2q-1) + z(2p, 2q) \tag{4}$$

$$z_{LH}(p,q) = -z(2p-1, 2q-1) - z(2p-1, 2q) \\ + z(2p, 2q-1) + z(2p, 2q) \tag{5}$$

$$z_{HL}(p,q) = -z(2p-1, 2q-1) + z(2p-1, 2q) \\ - z(2p, 2q-1) + z(2p, 2q) \tag{6}$$

$$z_{HH}(p,q) = z(2p-1, 2q-1) - z(2p-1, 2q) \\ - z(2p, 2q-1) + z(2p, 2q) \tag{7}$$

Four channels are used in DWT, whereas one channel is used in the max-pooling layer. All four channels of DWT are concatenated using Equation (8). After DWT, a convolutional layer having a filter size of 1 × 1 is applied to reduce channels of images generated through DWT. Furthermore, the output of both layers with equal channels is concatenated, and final output is provided to the successor block as shown in Figure 3.

$$DWT_{output} = concatenate(z_{LL}, z_{LH}, z_{HL}, z_{HH}) \tag{8}$$

3.2.5 | ASCPP bottleneck block

The ASCPP is used as the bottleneck of the proposed model. Three convolutional block attention modules (CBAM) [53] alongside four atrous convolution modules (ACM) are used in this model to increase the field of view to extract better features of small objects as shown in Figure 4. ACM is the combination of an atrous convolutional layer, a ReLU

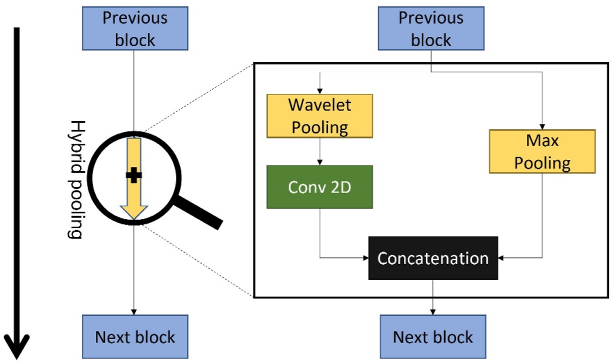

FIGURE 3 Combination of wavelet and max-pooling is introduced in the encoding block of the proposed model as Hybrid Pooling.

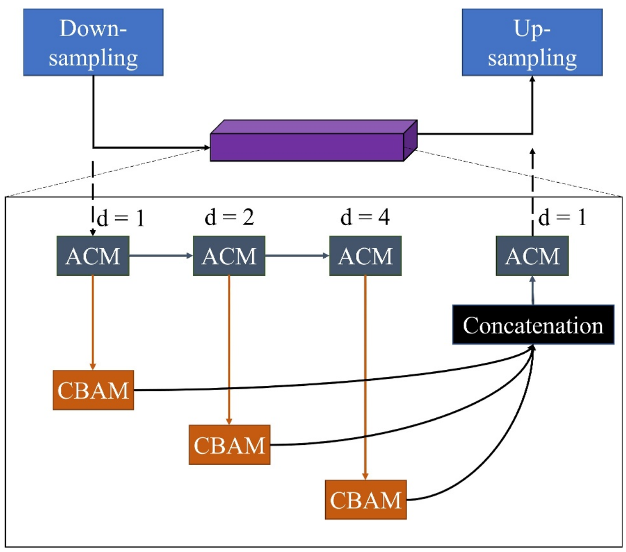

FIGURE 4 ASCPP bottleneck block is used as the combination of CBAM and ACM to focus on the location and class of the objects.

activation function, and a batch normalisation layer. Atrous modules are used to overcome the impact of max-pooling and convolutional layers on the size of objects and their spatial information. Kernel sizes of (3, 3) are used in all modules excluding the last ACM.

In CBAM, the sequences of the channel attention module and the spatial attention module are used. Channel attention utilised both max-pooling and average pooling followed by shared multi-layer perceptron. After the addition of both pooling layers, the sigmoid activation function is applied, and the channel attention map M_C is obtained by applying Equation (10). The concatenation of the channel attention map (M_C) and the input feature map (F) is provided to the spatial attention module as shown in Figure 5. Max-pooling and average pooling filters of size (7, 7) are applied in the spatial attention module using Equation (11). Channel-refined features are concatenated with the spatial attention map M_S to obtain refined features F' using Equation (9). The focus of channel attention is on 'what' meaningful information is given in the input image whereas spatial attention is applied to get

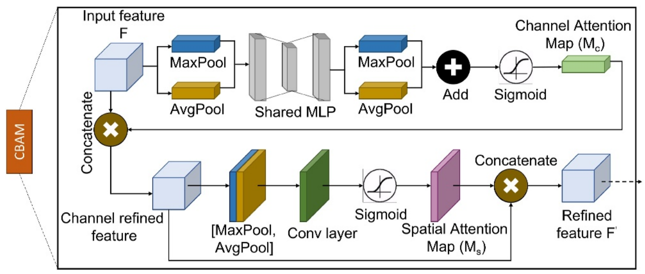

FIGURE 5 Convolutional block attention module (CBAM).

the location of meaningful information inside the input image, so it tries to give the information about 'where'.

$$F' = M_S(M_C(F) \otimes F) \otimes (M_C(F) \otimes F) \tag{9}$$

$$M_C(F) = \sigma(MLP(AvgPool(F)) + MLP(MaxPool(F))) \tag{10}$$

$$M_S(F) = \sigma\left(f^{(7\times7)}([AvgPool(F); MaxPool(F)])\right) \tag{11}$$

3.2.6 | Hybrid up-sampling

The proposed model utilises a hybrid approach of 2D up-sampling and IDWT to reconstruct images without losing information. 2D Up-sampling is the inverse of the pooling layer and increases the dimensionality by copying the previous level's values, but it does not restore the original features. On the other hand, IDWT is the reverse of DWT and can reconstruct images without the information loss. In the proposed method, images are reconstructed from the second level to the first level decomposition and then from the first level to the original image using all four channels. Equations (12–15) show the process of image reconstruction.

$$z(2p-1, 2q-1) = \frac{z_{LL}(p,q)}{4} - \frac{z_{LH}(p,q)}{4} - \frac{z_{HL}(p,q)}{4} + \frac{z_{HH}(p,q)}{4} \tag{12}$$

$$z(2p-1, 2q) = \frac{z_{LL}(p,q)}{4} - \frac{z_{LH}(p,q)}{4} + \frac{z_{HL}(p,q)}{4} - \frac{z_{HH}(p,q)}{4} \tag{13}$$

$$z(2p, 2q-1) = \frac{z_{LL}(p,q)}{4} + \frac{z_{LH}(p,q)}{4} - \frac{z_{HL}(p,q)}{4} - \frac{z_{HH}(p,q)}{4} \tag{14}$$

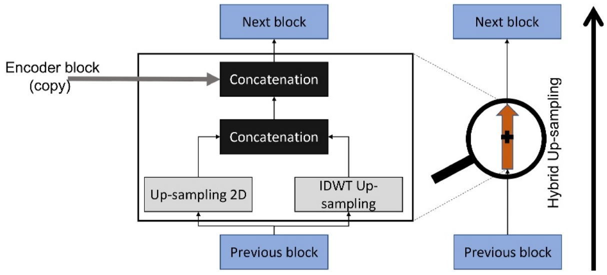

FIGURE 6 Combination of up-sampling and IDWT is introduced in the decoding block as Hybrid up-sampling.

$$z(2p,2q) = \frac{z_{LL}(p,q)}{4} + \frac{z_{LH}(p,q)}{4} + \frac{z_{HL}(p,q)}{4} + \frac{z_{HH}(p,q)}{4} \tag{15}$$

Where z is the image and (p, q) is the (p, q)th pixel value of z. The output of each location for all channels is concatenated using Equation (16). The output of both 2D up-sampling and IDWT is concatenated to produce a joint output of the hybrid up-sampling process. Images obtained through the hybrid up-sampling module are further concatenated with a copy of the encoder block of the upper level as shown in Figure 6.

$$IDWT_{output} = concatenate(z(2p-1,2q-1), z(2p-1,2q), z(2p,2q-1), z(2p,2q)) \tag{16}$$

3.2.7 | Watershed for boundaries identification and refinement

The watershed technique is a machine learning approach used to segment images by dividing them into different regions based on the intensity values of the pixels. In this model, it is used to separate different nuclei from each other by post-processing the predicted images. Initially, erosion and dilation are applied to determine the sure foreground and sure background of the image. The algorithm applies watersheds to the unknown area between the sure foreground and sure background, starting from the lowest intensity values and gradually filling in the surrounding pixels until it encounters a pixel with a higher intensity value. This process continues until the background in the image reaches the boundary of the foreground, resulting in a set of distinct regions corresponding to the nuclei. The technique is useful in the accurate counting of nuclei in histopathology images by identifying and refining touching boundaries of clustered nuclei.

4 | RESULTS AND DISCUSSIONS

The WaveSeg-UNet is a lightweight model proposed for identifying nuclei in histopathology data. It has fewer than one million parameters. The Adam optimiser with a learning rate of 0.0001 and a threshold of 0.5 is applied. The binary cross-entropy loss function and sigmoid activation function are used in the proposed model. The proposed model is trained up to 100 epochs on four datasets.

4.1 | Evaluation metrics

The F1 score and the Jaccard index are two evaluation metrics used for model evaluation. The F1 score is particularly useful for models that segment small or complex objects, as it is sensitive to boundary alignment. The F1 score is calculated using Equation (17). The Jaccard index measures the overlap between the prediction and the ground truth and ranges from 0 to 1, with higher values indicating better overlap. The Jaccard index is calculated using Equation (18).

$$F1 - score = \frac{2 * \mathrm{T_P}}{2 * \mathrm{T_P} + \mathrm{T_N} + \mathrm{F_P}} \tag{17}$$

$$JaccardIndex = \frac{Predicted_{value} \cap Actual_{value}}{Predicted_{value} \cup Actual_{value}} \tag{18}$$

4.2 | Ablation study

We investigated the proposed model through seven various combinations. In the initial investigation, we tested the standard U-Net model on all four datasets to get baseline results. This baseline model has 1.9 million parameters. Two other variations are performed by keeping the model's parameters constant. In the first variation, hybrid pooling and hybrid up-sampling are introduced. It is used to achieve true features of the image by preserving its definitions during various operations at different levels of the model. In another variation, the ASCPP bottleneck block is introduced to focus on the location and class of objects. We observed that the U-Net model having ASCPP and wavelet transform has better performance as compared to other variations with the same number of parameters. We named this variation as WaveSet-UNet+. In the next experiment, instead of keeping the parameters constant, we kept the components like hybrid pooling and ASCPP constant with various parameters and levels of encoder and decoder blocks. We changed the number of parameters of the model from 0.5 million to 35 million parameters. WaveSeg-UNet– has 0.5 million parameters, and WaveSet-UNet++ has 35 million parameters. The WaveSet-UNet– has three levels with 16 input parameters. The WaveSet-UNet++ has five levels with an input layer having 32 parameters. From all these variations, it is observed that the WaveSet-UNet model, having 1 million parameters, outperformed the other variations. We adopted the WaveSeg-UNet model as the proposed model with the same domain of transfer learning.

The standard U-Net has achieved an F1 score of 0.83, 0.81, 0.80, and 0.78 and Jaccard index odf 0.69, 0.67, 0.66, and 0.65 on Triple-Negative Breast Cancer (TNBC), BBBC039V1,

TABLE 1 Ablation study.

Ablations	Parameters (millions)	F1-score				Jaccard index			
		TNBC	BBBC039V1	MoNuSeg	PanNuke	TNBC	BBBC039V1	MoNuSeg	PanNuke
U-Net	1.9 M	0.83	0.81	0.80	0.78	0.69	0.67	0.66	0.65
U-Net with hybrid pooling and hybrid up-sampling	1.9 M	0.85	0.83	0.82	0.81	0.71	0.69	0.69	0.68
WaveSeg-UNet+	1.9 M	0.89	0.87	0.86	0.85	0.74	0.73	0.71	0.71
WaveSeg-UNet++	35 M	0.84	0.82	0.82	0.81	0.71	0.69	0.69	0.68
WaveSeg-UNet–	0.5 M	0.87	0.85	0.84	0.82	0.72	0.72	0.71	0.70
WaveSeg-UNet with transfer learning	1 M	0.92	0.90	0.88	0.87	0.76	0.76	0.75	0.74
The proposed WaveSeg-UNet	1 M	**0.94**	**0.92**	**0.91**	**0.90**	**0.80**	**0.79**	**0.77**	**0.75**

MoNuSeg, and PanNuke, respectively. WaveSeg-UNet++ is another variation of the proposed model. In this variation, we doubled the number of parameters in each level. Instead of improvisation, the model got overfit due to its complexity and high number of parameters. It achieved an F1 score of 0.84, 0.82, 0.82, and 0.81 and a Jaccard index 0.71, 0.69, 0.69, and 0.68 on TNBC, BBBC039V1, MoNuSeg, and PanNuke, respectively. WaveSeg-UNet– is another variation of a model which has 0.5 million parameters. It is the smallest version of the experimental variations. Experimenting this model on four datasets, we achieved an F1 score of 0.87, 0.85, 0.84, and 0.82 and the Jaccard index of 0.72, 0.72, 0.71, and 0.70, respectively. Alongside the standard U-Net model, we performed two other variations by keeping the parameters constant to 1.9 million. In first variation, we placed DWT in the encoding block and IDWT in the decoding block. Through this variation we achieved an F1 score of 0.85, 0.83, 0.82, and 0.81 and the Jaccard index 0.71, 0.69, 0.69, and 0.68, respectively. In the second variation named as WaveSeg-Unet+, we used ASCPP alongside DWT in the bottleneck of the model. This variation provided us with an F1 score of 0.89, 0.87, 0.86, 0.85 and the Jaccard index of 0.74, 0.73, 0.71, and 0.71, respectively. Finally, we achieved the best results on the same domain transfer learning of the proposed model having around 1 million parameters. The model has achieved an F1 score of 0.92, 0.90, 0.88, and 0.87 and the Jaccard index of 0.76, 0.76, 0.75, and 0.74 by using different domains of transfer learning and F1 score of 0.94, 0.92, 0.91, 0.90 and the Jaccard index of 0.80, 0.79, 0.77, and 0.75 by using pre-trained weights of the same domain. Results of these variations are shown in Table 1.

4.3 | Experimental results on multiple datasets

The proposed model is trained on four histopathology datasets including TNBC, BBBC039V1, MoNuSeg, and PanNuke. PanNuke is the most diverse dataset among all these. The model has achieved the highest F1 score of 0.94 and Jaccard index of 0.80 on the TNBC dataset. Similarly, it has secured an F1 score of 0.92, 0.91, and 0.90 on BBBC039V1, MoNuSeg, and PanNuke datasets, respectively. The Jaccard index of the model on these datasets is 0.79, 0.77, and 0.75, respectively. Results of the proposed model on these datasets are given in Table 2.

TABLE 2 Model generalisation on various datasets.

Datasets	F1 score	Jaccard index
TNBC	0.94	0.80
BBBC039V1	0.92	0.79
MoNuSeg	0.91	0.77
PanNuke	0.90	0.75

4.4 | Overall results on PanNuke dataset

Pre-trained weights of the proposed model on the same domain are used as transfer learning to retrain the model. The proposed model has achieved 0.91 train and 0.89 validation F1 score and 0.78 train and 0.75 validation Jaccard index. Variation within the dataset due to multiple organs made the dataset complex. The proposed model has shown a significant improvement in performance due to the wavelet transform in down-sampling and its inverse in up-sampling, atrous layers to focus on small object, spatial, and channel attentions to keep focussing on location and class of the identified objects.

4.5 | Organ-wise validation on test data

The performance of the proposed model varied depending on the organ due to the diversity of the data samples. The model performed well on most organs, except for the head and neck, which had a complex and diverse sample set with fewer samples. The model achieved the highest F1 score of 0.97 on the pancreatic organ, which had a high contrast between the background and foreground. The model achieved an F1 score of more than 0.90 on 13 organs out of 19

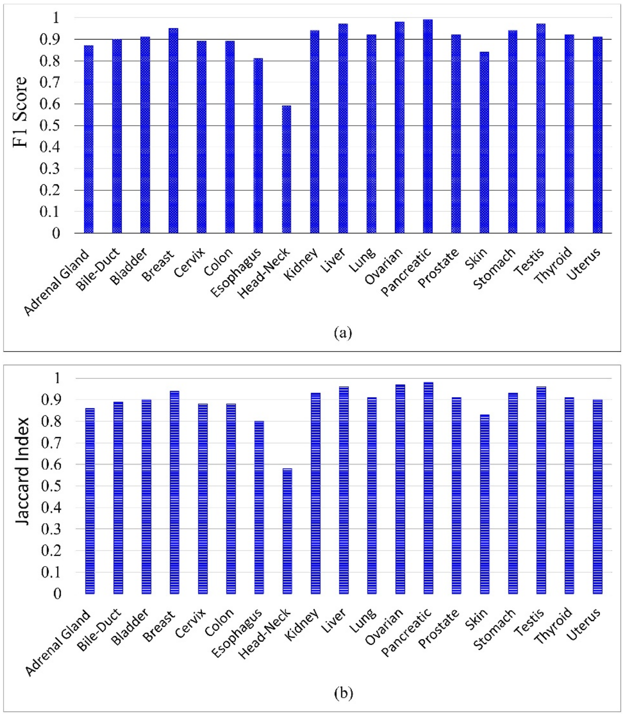

FIGURE 7 (a) F1 Score, (b) Jaccard index of all organs at test data.

TABLE 3 Performance of the proposed model at variable threshold values.

Threshold	F1 score	Jaccard index
0.2	0.94	0.81
0.3	0.93	0.79
0.4	0.91	0.77
0.5	0.89	0.75
0.6	0.87	0.72
0.7	0.86	0.71

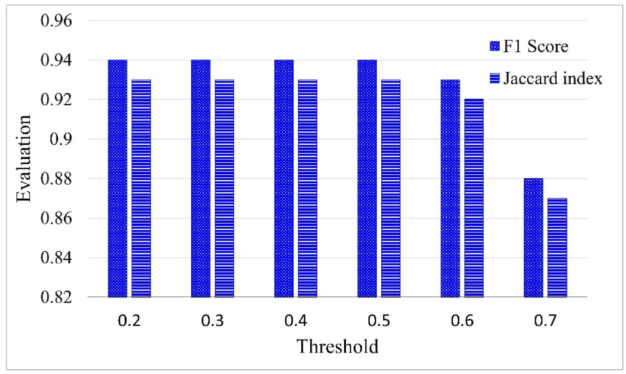

FIGURE 8 Performance of the proposed model at various threshold values.

and more than 0.80 on five out of the remaining six organs as shown in Table 5. The head and neck organs had the lowest F1 score of less than 0.70. The model also achieved the Jaccard index of more than or equal to 0.70 on 16 organs out of 19. The breast organ, which had the most frequent data samples, achieved the F1 score of 0.94 and the Jaccard index of 0.78. The performance of the model on test samples of all organs is shown in Figure 7.

4.6 | Results on various threshold values

Results of the proposed model are obtained at various threshold values as shown in Table 3. It is observed that at a low threshold value, the model has higher evaluation values. The performance of the model degrades as the threshold value increases. Comparison of all metrics at various threshold values is shown in Figure 8.

4.7 | Overlapped nuclei identification

In this study, initially, the WaveSeg-UNet predicts based on the input image. Error of the model is calculated by comparing predictions of the model with ground truths. In a post-processing stage, erosion and dilation of 2 and 5 iterations are used, respectively. An erosion operation is performed to confirm that the highlighted part of the predicted image is the sure foreground. Dilation is used to confirm the background of the predicted image. Similarly, in the next process, an unknown area that could be the area of possible touching boundaries is achieved by comparing sure foreground. The area of possible touching boundaries lies in between the nuclei and background. To make this unknown area known, a watershed technique is applied. The watershed identifies and refines boundaries. A special intensity value is given to identify boundary areas to draw nuclei boundaries and separate them from other nuclei as well as from the background. Results of identified touching boundaries are grey markers which are further converted to instances of segmented images using a conventional technique. Overlay of the identified objects is applied on the original images. Test results of the proposed model on all 19 organs of the PanNuke dataset are shown in Figures 9–12.

4.8 | Post-processing effects on nuclei counting

The watershed is a technique that divides an image into segments based on morphological information. It is used for boundary identification and refinement. In this study, the purpose of using this technique is to increase the mitotic count accuracy. Five images of the TNBC dataset having 371 actual nuclei are used for the evaluation of the model before and after boundary refinement. Similarly, 10 images from BBBC039V1 are used. The MoNuSeg dataset has seven organs. One image from each organ of this dataset is used for the evaluation of the

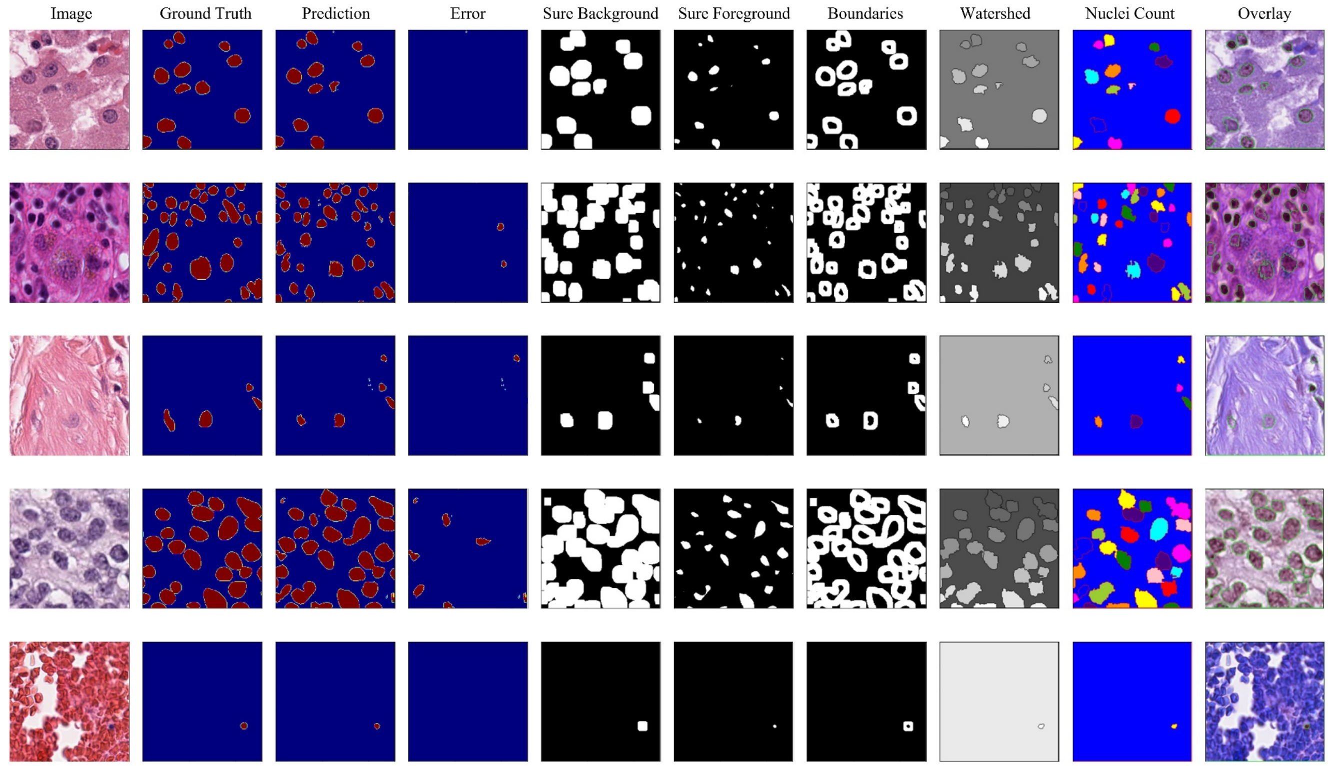

FIGURE 9 Predictions of the model on the test dataset of Adrenal Gland, Bile Duct, Bladder, Breast, and Cervix organs, respectively from top to bottom.

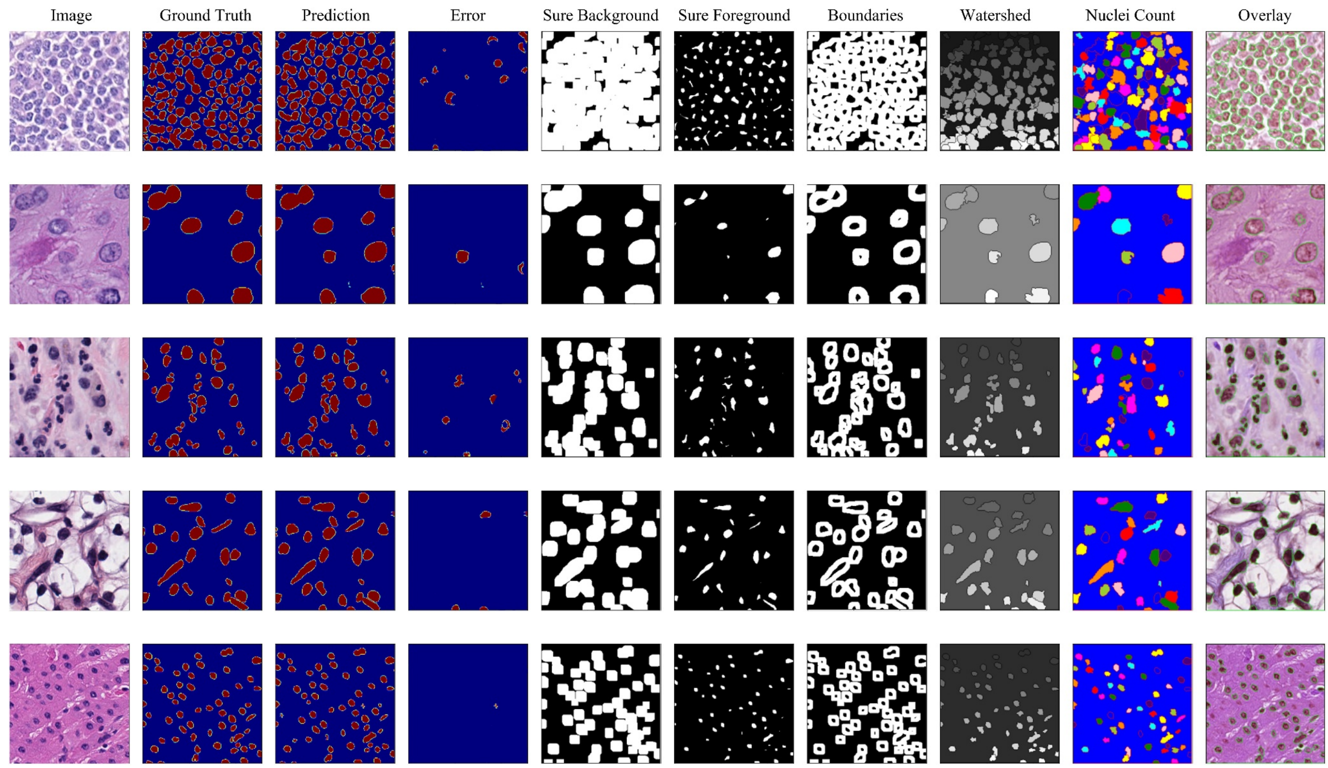

FIGURE 10 Predictions of the model on the test dataset of Colon, Oesophagus, Head–Neck, Kidney, and Liver organs, respectively from top to bottom.

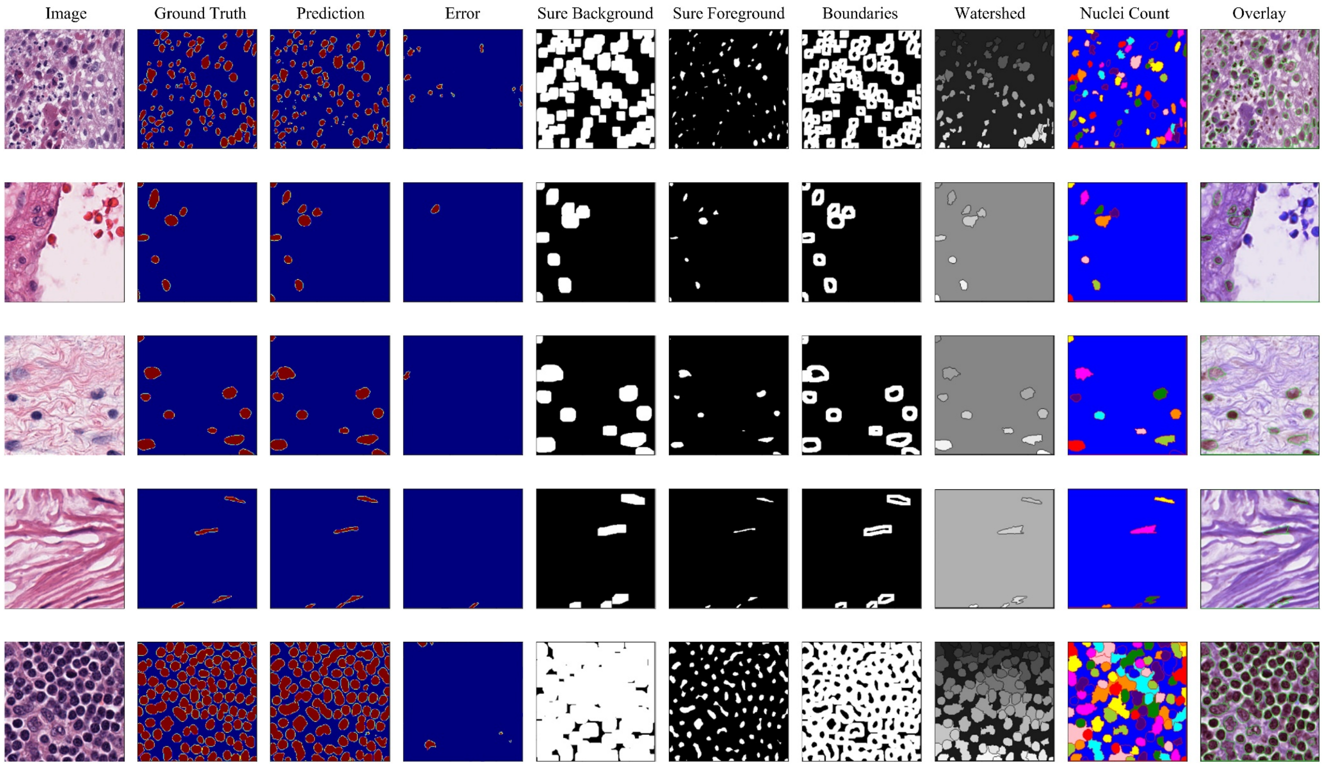

FIGURE 11 Predictions of the model on the test dataset of Lung, Ovarian, Pancreatic, Prostate, and Skin organs, respectively, from top to bottom.

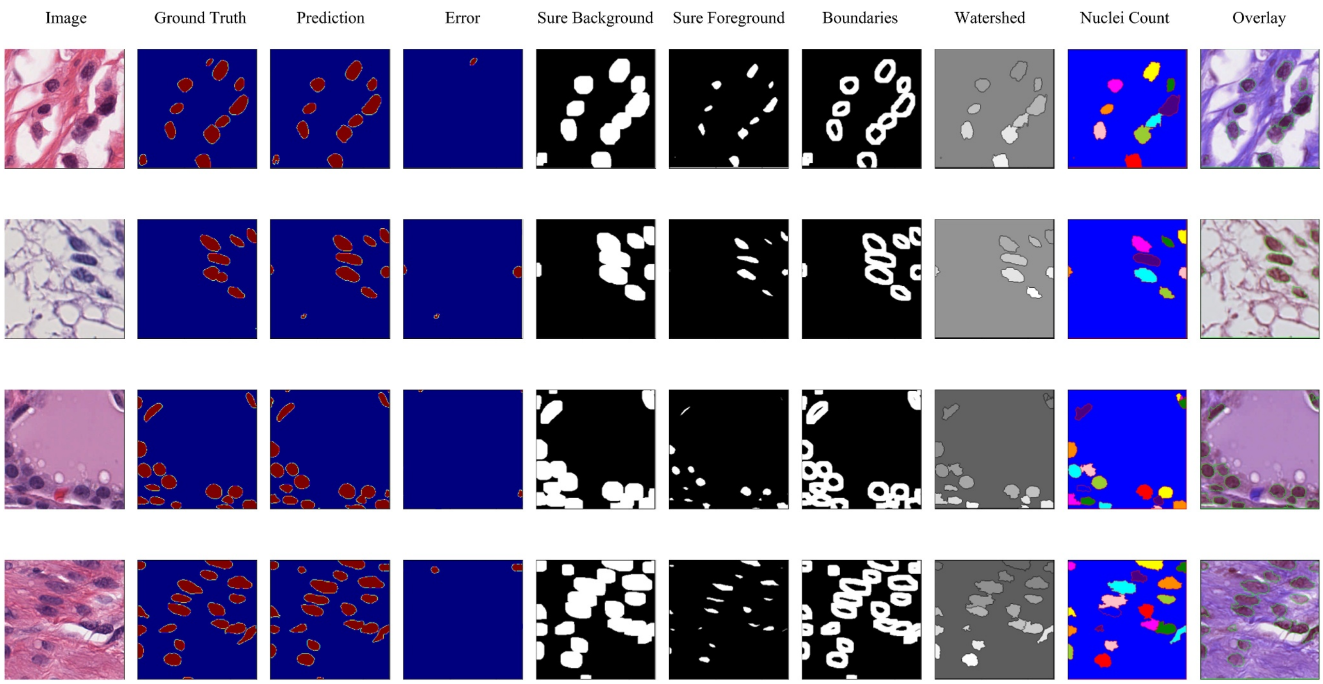

FIGURE 12 Predictions of the model on the test dataset of Stomach, Testis, Thyroid, and Uterus organs, respectively, from top to bottom.

model. On the other hand, five images from each organ of the PanNuke dataset are used. Results on all datasets and all organs are observed given in Table 4. A significant improvement is observed in the model after applying watershed boundaries identification and refinement technique.

4.9 | Comparison of organ-wise results with existing studies

The proposed model is compared with existing studies on 19 organs of the PanNuke dataset. It has comparatively low

TABLE 4 Results before and after post-processing.

Datasets	Organs	Test samples	Actual nuclei	Before post-processing: Predicted nuclei	Before post-processing: Misclassified nuclei	After post-processing: Predicted nuclei	After post-processing: Misclassified nuclei
TNBC	Breast	5	371	346	26	349	23
BBBC039V1	Breast	10	836	761	78	779	60
MoNuSeg	Bladder	1	52	49	5	51	3
	Breast	1	43	40	3	41	2
	Colon	1	31	31	2	33	1
	Kidney	1	31	29	2	30	1
	Liver	1	51	50	2	51	1
	Prostate	1	36	37	2	37	3
	Stomach	1	79	74	6	76	3
PanNuke	Adrenal gland	5	131	118	14	121	10
	Bile-duct	5	133	121	12	122	11
	Bladder	5	47	43	4	43	4
	Breast	5	133	128	6	131	3
	Cervix	5	75	77	3	76	1
	Colon	5	53	47	6	47	6
	Oesophagus	5	104	86	19	89	15
	Head-Neck	5	49	36	13	36	13
	Kidney	5	84	77	7	79	5
	Liver	5	307	292	16	193	15
	Lung	5	341	313	30	312	31
	Ovarian	5	220	211	11	213	8
	Pancreatic	5	89	87	2	87	2
	Prostate	5	76	71	5	70	6
	Skin	5	480	437	47	446	38
	Stomach	5	76	76	4	78	3
	Testis	5	23	23	0	23	0
	Thyroid	5	139	125	16	129	11
	Uterus	5	895	818	81	820	77

performance on the PanNuke dataset, so it is used as a base dataset to compare results with other studies. The proposed model is compared with three other state-of-the-art models: NucleiSegNet [39], DAN-NucNet [18], and DenseRes-Unet [15]. The proposed model outperforms the other models in terms of the F1 score on 17 organs, including adrenal gland, bile-duct, bladder, breast, cervix, colon, kidney, liver, lung, ovarian, pancreatic, prostate, skin, stomach, testis, thyroid, and uterus. However, on two organs, oesophagus and head–neck, DAN-NucNet has a higher F1 score as shown in Table 5. The Jaccard index of the proposed model is higher than the other models on 13 organs out of nineteen. DAN-NucNet has performed better on five organs including adrenal gland, bladder, cervix, oesophagus, and head–neck while DenseRes-Unet is found to be efficient on skin samples. The proposed model has the highest F1-score of 0.97 and the Jaccard index of 0.83 on the pancreatic organ. On average, the proposed model has an F1 score of 0.90 and a Jaccard index of 0.75, while NucleiSegNet has an F1 score of 0.83 and a Jaccard index of 0.72. Similarly, DAN-NucNet and DenseRes-Unet have F1 scores of 0.84 and 0.82 and Jaccard indices of 0.74 and 0.71, respectively.

4.10 | Comparison of overall results with existing studies

The proposed WaveSeg-UNet model has a significantly smaller number of parameters in comparison to other existing studies.

TABLE 5 Organ-wise comparison of results with existing studies.

	NucleiSegNet		DAN-NucNet		DenseRes-Unet		The proposed model	
Organs	**F1**	**JI**	**F1**	**JI**	**F1**	**JI**	**F1**	**JI**
Adrenal gland	0.82	0.72	0.84	**0.74**	0.79	0.68	**0.86**	0.72
Bile-duct	0.83	0.72	0.84	0.73	0.80	0.69	**0.90**	**0.76**
Bladder	0.84	0.74	0.87	**0.77**	0.80	0.70	**0.90**	0.76
Breast	0.83	0.72	0.83	0.72	0.82	0.71	**0.94**	**0.78**
Cervix	0.85	**0.76**	0.85	**0.76**	0.83	0.73	**0.89**	0.74
Colon	0.78	0.66	0.80	0.68	0.81	0.68	**0.87**	**0.72**
Kidney	0.83	0.73	0.84	0.75	0.78	0.67	**0.93**	**0.79**
Liver	0.85	0.74	0.86	0.77	0.86	0.73	**0.95**	**0.81**
Lung	0.78	0.65	0.82	0.69	0.79	0.67	**0.92**	**0.77**
Ovarian	0.85	0.74	0.85	0.75	0.84	0.72	**0.96**	**0.82**
Pancreatic	0.83	0.72	0.85	0.75	0.83	0.71	**0.97**	**0.83**
Prostate	0.83	0.72	0.84	0.74	0.84	0.73	**0.92**	**0.79**
Stomach	0.87	0.77	0.87	0.78	0.88	0.77	**0.93**	**0.79**
Testis	0.84	0.73	0.86	0.77	0.86	0.75	**0.95**	**0.81**
Thyroid	0.84	0.74	0.86	0.76	0.87	**0.77**	**0.91**	**0.77**
Uterus	0.84	0.73	0.84	0.73	0.81	0.72	**0.90**	**0.76**
Average	0.83	0.72	0.84	0.74	0.82	0.71	**0.90**	**0.75**

TABLE 6 Comparison of results with existing studies.

Existing studies	F1 score	Jaccard index
U-Net [54]	0.78	0.65
UNet++ [55]	0.78	0.66
DIST [33]	0.72	0.55
MicroNet [56]	0.81	0.70
ASPP UNet [40]	0.76	0.63
SCPP-Net [57]	0.77	0.65
NucleiSegNet [39]	0.83	0.72
DenseRes-Unet [15]	0.82	0.71
DAN-NucNet [18]	0.84	0.74
The proposed model	**0.90**	**0.75**

With only 0.9 million parameters, it has less than 50% of the parameters of the closest model, which is DenseRes-Unet with 2.2 million parameters. It outperformed state-of-the-art existing studies as shown in Table 6. Jaccard index and F1 score of the model are compared with U-Net [54], UNet++ [55], DIST [33], MicroNet [56], ASPP Unet [40], SCPP-Net [57], NucleiSegNet [39], DenseRes-Unet [15], and DAN-NucNet [18]. The DAN-NucNet [18] is the second high performing model which has 0.84 F1 score and 0.74 Jaccard index. The DIST [33] has the lowest performance on the multi-organ PanNuke dataset. It has 0.72 F1 score and 0.55 Jaccard index. From the rest of the studies, the U-Net [54], UNet++ [55], MicroNet [56], ASPP UNet [40], SCPP-Net [57], NucleiSegNet [39], and DenseRes-Unet [15] have F1 scores of 0.78, 0.78, 0.81, 0.76, 0.77, 0.83, and 0.82 and the Jaccard indices of 0.65, 0.66, 0.70, 0.63, 0.65, 0.72, and 0.71, respectively.

5 | CONCLUSION AND FUTURE WORK

In this study, the WaveSeg-UNet is proposed for overlapped nuclei segmentation of 19 organs. The model is designed to overcome the limitations of small datasets using the same domain transfer learning, which has advantages over different domains of transfer learning. The WaveSeg-UNet is a light-weight model with 0.9 million parameters, which uses three encoder and three decoder levels with a residual block in each level to extract features. The hybrid pooling is used in down-sampling to preserve the shapes of objects, and the ASCPP block is used in bottleneck to increase the receptive field for better feature extraction. In the proposed model, spatial and channel attention are applied to focus on the location and class of the object. The model achieved a 0.90 F1 score and a 0.75 Jaccard index, which outperformed state-of-the-art models. Finally, watershed is used as a post-processing technique to identify and modify touching boundaries of nuclei. In the future, deep learning techniques need to be introduced for overlapped multi-class nuclei segmentation.

ACKNOWLEDGEMENTS

The authors express their gratitude to their affiliated universities for providing financial support to accomplish this research work.

CONFLICT OF INTEREST STATEMENT

The authors have no conflicts of interest to declare that are relevant to the content of this article.

DATA AVAILABILITY STATEMENT

The data will be available upon request to the corresponding author.

CODE AVAILABILITY

The code will be available upon request to the corresponding author.

ORCID

Muhammad Faheem https://orcid.org/0000-0003-4628-4486

REFERENCES

1. Agbley, B.Y.L., et al.: Federated fusion of magnified histopathological images for breast tumor classification in the internet of medical things. IEEE J. Biomed. Health Inform. (2023)
2. Xing, F., et al.: Bidirectional mapping-based domain adaptation for nucleus detection in cross-modality microscopy images. IEEE Trans. Med. Imag. 40(10), 2880–2896 (2020). https://doi.org/10.1109/TMI.2020.3042789
3. Li, C., et al.: Weakly supervised mitosis detection in breast histopathology images using concentric loss. Med. Image Anal. 53, 165–178 (2019). https://doi.org/10.1016/j.media.2019.01.013
4. Xing, F., Xie, Y., Yang, L.: An automatic learning-based framework for robust nucleus segmentation. IEEE Trans. Med. Imag. 35(2), 550–566 (2015). https://doi.org/10.1109/TMI.2015.2481436
5. Song, Y., et al.: Accurate cervical cell segmentation from overlapping clumps in pap smear images. IEEE Trans. Med. Imag. 36(1), 288–300 (2016). https://doi.org/10.1109/TMI.2016.2606380
6. Wu, J., et al.: A medically assisted model for precise segmentation of osteosarcoma nuclei on pathological images. IEEE J. Biomed. Health Inform. 27(8), 3982–3993 (2023). https://doi.org/10.1109/jbhi.2023.3278303
7. Mahmood, F., et al.: Deep adversarial training for multi-organ nuclei segmentation in histopathology images. IEEE Trans. Med. Imag. 39(11), 3257–3267 (2019). https://doi.org/10.1109/TMI.2019.2927182
8. Qu, H., et al.: Weakly supervised deep nuclei segmentation using partial points annotation in histopathology images. IEEE Trans. Med. Imag. 39(11), 3655–3666 (2020). https://doi.org/10.1109/TMI.2020.3002244
9. Ali, G., et al.: A hybrid convolutional neural network model for automatic diabetic retinopathy classification from fundus images. IEEE J. Trans. Eng. Health Med. 11(1), 341–350 (2023). https://doi.org/10.1109/jtehm.2023.3282104
10. Khan, A.A., et al.: D2pam: epileptic seizures prediction using adversarial deep dual patch attention mechanism. CAAI Trans. Intell. Technol. 8(3), 755–769 (2023). https://doi.org/10.1049/cit2.12261
11. Ahmad, I., et al.: Autism spectrum disorder detection using facial images: a performance comparison of pretrained convolutional neural networks. Healthc. Technol. Lett., 1–13 (2024). https://doi.org/10.1049/htl2.12073
12. Aslam, M.Z., et al.: Aml-net: attention-based multi-scale lightweight model for brain tumour segmentation in internet of medical things. CAAI Trans. Intell. Technol., 1–17 (2024). https://doi.org/10.1049/cit2.12278
13. Alarood, A.A., et al.: Secure medical image transmission using deep neural network in e-health applications. Healthc. Technol. Lett. 10(4), 87–98 (2023). https://doi.org/10.1049/htl2.12049
14. Song, J., Xiao, L., Lian, Z.: Contour-seed pairs learning-based framework for simultaneously detecting and segmenting various overlapping cells/nuclei in microscopy images. IEEE Trans. Image Process. 27(12), 5759–5774 (2018). https://doi.org/10.1109/TIP.2018.2857001
15. Kiran, I., et al.: DenseRes-Unet: segmentation of overlapped/clustered nuclei from multi organ histopathology images. Comput. Biol. Med. 143, 105267 (2022). https://doi.org/10.1016/j.compbiomed.2022.105267
16. Song, J., Xiao, L., Lian, Z.: Boundary-to-marker evidence-controlled segmentation and MDL-based contour inference for overlapping nuclei. IEEE J. Biomed. Health Inform. 21(2), 451–464 (2015). https://doi.org/10.1109/JBHI.2015.2504422
17. Li, K., et al.: Weakly supervised histopathology image segmentation with self-attention. Med. Image Anal., 102791 (2023). https://doi.org/10.1016/j.media.2023.102791
18. Ahmad, I., et al.: Dan-nucnet: a dual attention based framework for nuclei segmentation in cancer histology images under wild clinical conditions. Expert Syst. Appl. 213, 118945 (2023). https://doi.org/10.1016/j.eswa.2022.118945
19. Wu, H., et al.: Feature masking on non-overlapping regions for detecting dense cells in blood smear image. IEEE Trans. Med. Imag. (2023). https://doi.org/10.1109/TMI.2023.3234688
20. Ali, S., Madabhushi, A.: An integrated region-, boundary-, shape-based active contour for multiple object overlap resolution in histological imagery. IEEE Trans. Med. Imag. 31(7), 1448–1460 (2012). https://doi.org/10.1109/TMI.2012.2190089
21. Al-Kofahi, Y., et al.: Improved automatic detection and segmentation of cell nuclei in histopathology images. IEEE Trans. Biomed. Eng. 57(4), 841–852 (2009). https://doi.org/10.1109/TBME.2009.2035102
22. Kumar, N., et al.: A multi-organ nucleus segmentation challenge. IEEE Trans. Med. Imag. 39(5), 1380–1391 (2019). https://doi.org/10.1109/TMI.2019.2947628
23. Kong, H., Gurcan, M., Belkacem-Boussaid, K.: Partitioning histopathological images: an integrated framework for supervised color-texture segmentation and cell splitting. IEEE Trans. Med. Imag. 30(9), 1661–1677 (2011). https://doi.org/10.1109/TMI.2011.2141674
24. Chang, H., et al.: Invariant delineation of nuclear architecture in glioblastoma multiforme for clinical and molecular association. IEEE Trans. Med. Imag. 32(4), 670–682 (2012). https://doi.org/10.1109/TMI.2012.2231420
25. Ullah, K., et al.: Machine learning-based prediction of osteoporosis in postmenopausal women with clinical examined features: a quantitative clinical study. Health Sci. Rep. 6(10), 1–10 (2023)
26. Rashid, J., et al.: Mouth and oral disease classification using inception-resnetv2 method. Multimed. Tool. Appl., 1–19 (2023)
27. Khan, A.A., et al.: Dual-3dm 3-ad: mixed transformer based semantic segmentation and triplet pre-processing for early multi-class alzheimer's diagnosis. IEEE Trans. Neural Syst. Rehabil. Eng. 32, 696–707 (2024)
28. Kumar, N., et al.: A dataset and a technique for generalized nuclear segmentation for computational pathology. IEEE Trans. Med. Imag. 36(7), 1550–1560 (2017). https://doi.org/10.1109/TMI.2017.2677499
29. Moen, E., et al.: Deep learning for cellular image analysis. Nat. Methods 16(12), 1233–1246 (2019). https://doi.org/10.1038/s41592-019-0403-1
30. Akram, A., et al.: Segmentation and classification of skin lesions using hybrid deep learning method in the internet of medical things. Skin Res. Technol. 29(11), 1–14 (2023)
31. Blose, M., et al.: Scalable hybrid switching-driven software defined networking issue: from the perspective of reinforcement learning. IEEE Access (2024)
32. Cui, Y., et al.: A deep learning algorithm for one-step contour aware nuclei segmentation of histopathology images. Med. Biol. Eng. Comput. 57(9), 2027–2043 (2019). https://doi.org/10.1007/s11517-019-02008-8
33. Naylor, P., et al.: Segmentation of nuclei in histopathology images by deep regression of the distance map. IEEE Trans. Med. Imag. 38(2), 448–459 (2018). https://doi.org/10.1109/TMI.2018.2865709

34. Khoshdeli, M., Winkelmaier, G., Parvin, B.: Fusion of encoder-decoder deep networks improves delineation of multiple nuclear phenotypes. BMC Bioinform. 19(1), 1–11 (2018). https://doi.org/10.1186/s12859-018-2285-0
35. Sirinukunwattana, K., et al.: Locality sensitive deep learning for detection and classification of nuclei in routine colon cancer histology images. IEEE Trans. Med. Imag. 35(5), 1196–1206 (2016). https://doi.org/10.1109/TMI.2016.2525803
36. Zhou, Z., et al.: Unet++: redesigning skip connections to exploit multiscale features in image segmentation. IEEE Trans. Med. Imag. 39(6), 1856–1867 (2019). https://doi.org/10.1109/TMI.2019.2959609
37. Yi, J., et al.: Attentive neural cell instance segmentation. Med. Image Anal. 55, 228–240 (2019). https://doi.org/10.1016/j.media.2019.05.004
38. Liang, H., et al.: A region-based convolutional network for nuclei detection and segmentation in microscopy images. Biomed. Signal Process Control 71, 103276 (2022). https://doi.org/10.1016/j.bspc.2021.103276
39. Lal, S., et al.: NucleiSegNet: robust deep learning architecture for the nuclei segmentation of liver cancer histopathology images. Comput. Biol. Med. 128, 104075 (2021). https://doi.org/10.1016/j.compbiomed.2020.104075
40. Wan, T., et al.: Robust nuclei segmentation in histopathology using ASPPU-Net and boundary refinement. Neurocomputing 408, 144–156 (2020). https://doi.org/10.1016/j.neucom.2019.08.103
41. Wang, E.K., et al.: Multi-path dilated residual network for nuclei segmentation and detection. Cells 8(5), 499 (2019). https://doi.org/10.3390/cells8050499
42. Khan, H.U., et al.: SMDetector: small mitotic detector in histopathology images using faster R-CNN with dilated convolutions in backbone model. Biomed. Signal Process Control 81, 104414 (2023). https://doi.org/10.1016/j.bspc.2022.104414
43. Ding, H., et al.: Multi-scale fully convolutional network for gland segmentation using three-class classification. Neurocomputing 380, 150–161 (2020). https://doi.org/10.1016/j.neucom.2019.10.097
44. Raza, B., et al.: Autonomic performance prediction framework for data warehouse queries using lazy learning approach. Appl. Soft Comput. 91, 106216 (2020)
45. Graham, S., et al.: Hover-net: simultaneous segmentation and classification of nuclei in multi-tissue histology images. Med. Image Anal. 58, 101563 (2019). https://doi.org/10.1016/j.media.2019.101563
46. Yao, K., et al.: PointNu-net: keypoint-assisted convolutional neural network for simultaneous multi-tissue histology nuclei segmentation and classification. IEEE Trans. Emerg. Top. Comput. Intell. 8(1), 802–813 (2023). https://doi.org/10.1109/tetci.2023.3281864
47. Ahmad, I., Israr, S.M., Islam, Z.Ul: A three in one bottom-up framework for simultaneous semantic segmentation, instance segmentation and classification of multi-organ nuclei in digital cancer histology. arXiv preprint (2023). arXiv:2308.11179
48. Graham, S., et al.: One model is all you need: multi-task learning enables simultaneous histology image segmentation and classification. Med. Image Anal. 83, 102685 (2023). https://doi.org/10.1016/j.media.2022.102685
49. Zhao, B., et al.: Triple U-net: hematoxylin-aware nuclei segmentation with progressive dense feature aggregation. Med. Image Anal. 65, 101786 (2020). https://doi.org/10.1016/j.media.2020.101786
50. Gamper, J., et al.: Pannuke: an open pan-cancer histology dataset for nuclei instance segmentation and classification. In: European Congress on Digital Pathology, pp. 11–19. Springer (2019). https://doi.org/10.1007/978-3-030-23937-4_2
51. Gamper, J., et al.: Pannuke dataset extension, insights and baselines. arXiv preprint (2020). arXiv:2003.10778
52. Liu, P., et al.: Multi-level wavelet convolutional neural networks. IEEE Access 7, 74973–74985 (2019). https://doi.org/10.1109/ACCESS.2019.2921451
53. Woo, S., et al.: Cbam: convolutional block attention module. In: Proceedings of the European Conference on Computer Vision (ECCV), pp. 3–19 (2018)
54. Ronneberger, O., Fischer, P., Brox, T.: U-net: convolutional networks for biomedical image segmentation. In: International Conference on Medical Image Computing and Computer-Assisted Intervention, pp. 234–241. Springer (2015). https://doi.org/10.1007/978-3-319-24574-4_28
55. Zhou, Z., et al.: Unet++: a nested u-net architecture for medical image segmentation. In: Deep Learning in Medical Image Analysis and Multimodal Learning for Clinical Decision Support, pp. 3–11. Springer (2018). https://doi.org/10.1007/978-3-030-00889-5_1
56. Raza, S.E.A., et al.: Micro-net: a unified model for segmentation of various objects in microscopy images. Med. Image Anal. 52, 160–173 (2019). https://doi.org/10.1016/j.media.2018.12.003
57. Chanchal, A.K., et al.: Efficient and robust deep learning architecture for segmentation of kidney and breast histopathology images. Comput. Electr. Eng. 92, 107177 (2021). https://doi.org/10.1016/j.compeleceng.2021.107177

How to cite this article: Khan, H.U., et al.: WaveSeg-UNet model for overlapped nuclei segmentation from multi-organ histopathology images. CAAI Trans. Intell. Technol. 1–15 (2024). https://doi.org/10.1049/cit2.12351